The effect of Cl, Br, and F on high-temperature corrosion of heat-transfer alloys

Eriksson, Jan-Erik; Lehmusto, Juho; Dirbeba, Meheretu Jaleta; Silvander, Linus; Lindberg, Daniel; Hupa, Leena

Published in:
Fuel

DOI:
10.1016/j.fuel.2023.128516

Published: 15/09/2023

Document Version
Final published version

Document License
CC BY

Fuel 348 (2023) 128516

Contents lists available at ScienceDirect

Fuel

journal homepage: www.elsevier.com/locate/fuel

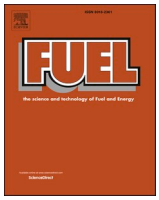

Full Length Article

The effect of Cl, Br, and F on high-temperature corrosion of heat-transfer alloys

J.-E. Eriksson [a,*], J. Lehmusto [a], M. Dirbeba [a], L. Silvander [a], D. Lindberg [b], L. Hupa [a]

[a] Johan Gadolin Process Chemistry Centre, Åbo Akademi University, Turku, Finland
[b] Department of Chemical and Metallurgical Engineering, Aalto University, Espoo, Finland

ARTICLE INFO

Keywords:
Waste combustion
High-temperature corrosion
Alkali halides
Melt formation
Heat-transfer materials

ABSTRACT

The impact of small alkali halide additions on the melting behavior and corrosivity of a synthetic sulfate deposit at 500, 550, and 600 °C was investigated. Three differently alloyed commercial heat-transfer materials; low-alloyed 10CrMo9-10, stainless AISI 347, and high-alloyed Sanicro 28, were studied. The samples were exposed for 168 h in a tube furnace to a $K_2SO_4 + Na_2SO_4$ mixture containing 0.85 mol% KCl, KBr, or KF. The extent of material degradation was determined by weight loss measurements, while the morphology, thickness, and composition of the formed oxide scale were characterized with SEM-EDS. Additionally, the melting behavior of the mixtures was studied with TG-DTA. It could be concluded that already small amounts of reactive alkali halides in an otherwise inert $K_2SO_4 + Na_2SO_4$ mixture change significantly the corrosion and melting behavior of the mixture.

1. Introduction

The strive for more sustainable utilization of waste-derived power production keeps the interest in biomass and municipal solid waste growing. When addressing biomass such as forest or agricultural residues, they can be considered CO_2-neutral fuels, because the same amount of CO_2 is consumed in photosynthesis during the growth of biomass as is released through combustion. Furthermore, power production through waste combustion provides a noteworthy alternative for landfilling, which has become chargeable in EU countries and therefore, a cost issue. However, to be a realistic and noteworthy alternative to fossil fuels, the steam temperatures in waste-fired power plants have to be sufficiently high. As a rule of thumb, it can be said that every 10 °C rise in the steam temperature results in an approximate increase of 2 % in power production efficiency [1,2]. The maximal steam temperature is dictated mainly by the chemical composition of the combusted fuel: steam temperatures above 600 °C are applied in boilers fired with coal and gas whereas firing lower-grade fuels like biomass and waste requires significantly lower steam temperatures (around 500 °C). The main reason for these lower steam temperatures is the presence of corrosive species in biomass and waste. After being released in combustion, these species may interact with various heat-transfer surfaces, resulting in material degradation, whose severity is dependent on the material surface temperature. To slow down or reduce corrosion, power plants using biomass and/or waste as fuel have been forced to operate at lower steam temperatures, which reduces power production efficiency. Therefore, more efficient ways to prevent corrosion are needed, so that power plants using biomass and waste-derived fuels can operate at higher steam temperatures.

Since the chemical composition of waste may vary greatly, the type and amount of corrosive species depend on the source of the waste, but alkali halides are generally considered to be among the most aggressive species. Regarding biomass, potassium (to some extent, also sodium) and chlorine have been identified as the main cause of high-temperature corrosion, mainly in the form of potassium (KCl) or sodium chloride (NaCl) [i.a. 3–6]. New alternatives for renewable fuels have emerged on the side of biomass-based fuels, which have been utilized longer in the field of power production. Solid recovered fuels (SRFs) are an example of these fuels that may contain traces of brominated flame retardants (BFR) and/or high-performance plastics known as fluoropolymers which can be found in various commodities. Such feedstocks are very heterogeneous from their chemical composition, containing Pb, Zn, F, and Br, for example [7–11]. In addition to potassium and chlorine, these elements are known to create fly ash with a low melting point, making the ash more likely to adhere to heat-transfer surfaces, increasing the risk of corrosion [1,12,13]. The presence of these elements in current waste-

* Corresponding author.
E-mail address: jan-erik.eriksson@abo.fi (J.-E. Eriksson).

https://doi.org/10.1016/j.fuel.2023.128516
Received 30 November 2022; Received in revised form 12 April 2023; Accepted 21 April 2023
Available online 29 April 2023

derived fuels generates a new kind of high-temperature chemistry in the form of reactions occurring in the deposits forming on the heat-transfer surfaces.

In the case of chromia based alloys, the KCl-induced high-temperature corrosion reaction is considered to initiate, when the protective chromia (Cr_2O_3) layer at the steel surface is destroyed through potassium chromate (K_2CrO_4) formation, resulting in Cr-depletion of the surface oxide, making it more prone to further material degradation (Eq. 1a for dry and 1b for humid conditions) [15]. The few studies addressing KBr found it corrosive to various commercial heat-transfer alloys in the tested temperature range of 400–600 °C [11–14]. The severity of corrosion depended on alloy quality, prevailed temperature, and atmosphere. It was proposed that the reaction between KBr and steel (Eq. 2a for dry and 2b for humid conditions) proceeds similarly to the KCl-induced corrosion. In the equations, only the first reactions with K_2CrO_4 as a solid intermediate have been presented. In other words, the presented reactions do not end in the formation of the intermediates but continue further. It is also worth mentioning that, based on the Gibbs free energy values, the presented reactions are non-spontaneous.

$$8KCl(s) + 2Cr_2O_3(s) + 5O_2(g) \rightarrow 4K_2CrO_4(s) + 4Cl_2(g),\ \Delta G = 281161\ J\ (at\ 550\ °C) \quad (1a)$$

$$8KCl(s) + 2Cr_2O_3(s) + 3O_2(g) + 4H_2O(g) \rightarrow 4K_2CrO_4(s) + 8HCl(g),\ \Delta G = 293184\ J\ (at\ 550\ °C) \quad (1b)$$

$$8KBr(s) + 2Cr_2O_3(s) + 5O_2(g) \rightarrow 4K_2CrO_4(s) + 4Br_2(g),\ \Delta G = 77184\ J\ (at\ 550\ °C) \quad (2a)$$

$$8KBr(s) + 2Cr_2O_3(s) + 3O_2(g) + 4H_2O(g) \rightarrow 4K_2CrO_4(s) + 8HBr(g),\ \Delta G = 409684\ J\ (at\ 550\ °C) \quad (2b)$$

Since the chemical compositions of waste-derived fuels are becoming more complex, information about the synergistic effect of alkali halides and other common species in deposits is needed. Although the possible corrosivity of alkali halides other than KCl has been identified [16] only a few studies are addressing the corrosive properties of KBr and KF [11,14] In these studies, the corrosive effect of pure alkali halides was investigated, but since the amount of especially bromine and fluorine in waste fuels is usually low, it is not yet fully understood how the relatively small amounts of these impurities can dramatically change the oxidation behavior of the heat-transfer materials. Therefore, more information is needed about the potential role of small alkali halide amounts in melt formation and reaction mechanics regarding high-temperature corrosion under conditions relevant to biomass and waste combustion.

The study contained two main goals: i) to shed more light on the high-temperature corrosion behavior of three halogens found in anthropogenic waste and ii) to study the possible correlation between mass loss and the oxide layer thickness of each alloy. The goals were addressed by adding small amounts of alkali halides to a carrier salt. The carrier salt consisted of K_2SO_4 and Na_2SO_4 and was chosen because it is known to be non-corrosive at studied temperatures. By doing so, the effect of the small addition of each alkali halide both in corrosivity and melting behavior could be pointed out. To better understand the potential role of sulfates in melt formation and in reaction mechanics, the new results were also compared with results from a similar study carried out with pure alkali halides. Furthermore, the current understanding of the melting behavior of alkali halogen-sulfate mixtures is complemented.

2. Materials and methods

2.1. Materials

The heat-transfer materials chosen for the experiments were austenitic stainless steels AISI 347 and Sanicro 28, and a ferritic steel 10CrMo9-10. All tested materials were commercial and delivered by different Finnish boiler manufacturers. The nominal elemental compositions of the studied materials are presented in Table 1.

The sample pieces were pre-treated as described by Skrifvars et al. [5]. For every experiment, two pieces of each steel were cut to ~ 20 × 20 mm pieces with a thickness of ~ 5 mm and polished with gradually finer SiC papers. The final touch was made with grit 500 SiC paper using ethanol. Then, the pieces were pre-oxidized in the air at 200 °C for 24 h. The mild pre-oxidation ensures that the surface is smooth and in a reproducible state at the beginning of each experiment. With the studied steels, the oxide thickness after the applied pre-oxidation is 20 nm at most [17], so its share of the final oxide thickness after a 168-hour experiment at 500 °C and above can be considered negligible. After pre-oxidation, one sample of each steel for every experiment was weighed 3 times using a Mettler AJ150 scale and the average value was recorded.

2.2. Salt mixtures

Four different salt mixtures were tested. A pure mixture of K_2SO_4 + Na_2SO_4 was used as a carrier and a reference mixture. The three halogens, Cl, Br, or F were added to the carrier as potassium halides in 0.85 mol% mixtures. After the potassium halide addition, the salt mixture was molten to ensure homogeneity, cooled, molten again, and finally ground and sieved to a fraction of 32–100 μm.

The melting behavior of each mixture was studied with a Simultaneous Thermal Analyzer (DSC-TG, TA Instruments SDT Q600) by heating the sample in N_2 (flow rate 100mlmin^{-1}) up to 600 °C (K_2SO_4 + Na_2SO_4 + KBr and K_2SO_4 + Na_2SO_4 + KCl), 750 °C (K_2SO_4 + Na_2SO_4 + KF), or 900 °C (K_2SO_4 + Na_2SO_4).

2.3. High-temperature corrosion experiments

The corrosion experiments for each studied salt mixture were carried out separately at three different temperatures, i.e., 500, 550, and 600 °C. Two pieces of each material were simultaneously exposed in a horizontal Carbolite tube furnace equipped with an inner alumina tube. A gas-tight quartz tube with gas inlets and outlets was inserted inside the inner alumina tube. This setup enabled controlled atmospheres in the tube reactor. (Fig. 1). With all experiments, a gas flow rate of 0.2 l/min at NTP was used.

Before the furnace exposures, 0.250 g of salt was placed on the surface of each sample using a mold. The samples were then inserted into the furnace on a sample holder at room temperature. During the exposures, the temperature was monitored with thermocouples attached to the sample holder, and sample temperatures were maintained within ± 2 °C from the target temperature. The heating was carried out at a rate of 8 °Cmin^{-1} and an N_2 flow of 0.5 lmin^{-1} was used to ensure an inert atmosphere before reaching the target temperature. Once the target temperature was reached, nitrogen was replaced by an airflow of 0.2 lmin^{-1}. The exposure time at the target temperature was 168 h, after which the furnace was shut off and cooled to room temperature in an N_2 flow of 0.5 lmin^{-1}.

Table 1
Nominal composition (wt%) of the tested heat-transfer materials. Only the main components are listed.

	10CrMo9-10	AISI347	Sanicro28
Fe	95,96	68,74	36,11
Cr	2,24	18,08	27,36
Mo	1,00		
Mn	0,45	0,92	1,15
Si	0,25	0,46	0,46
Ni		10,92	31,38
C	0,07	0,04	0,01

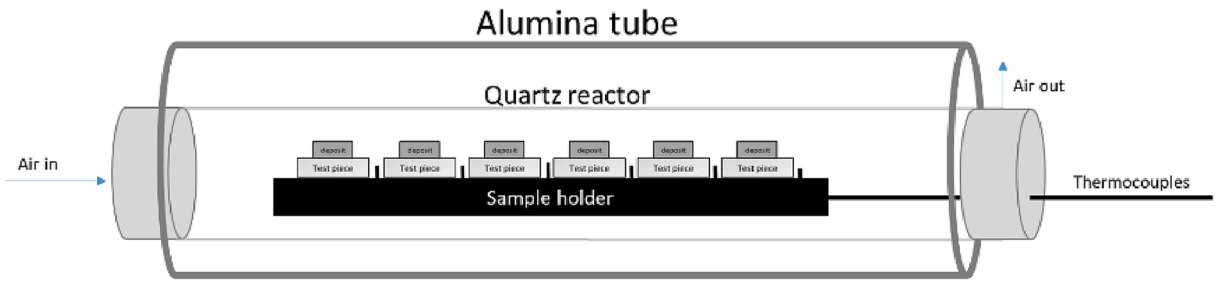

Fig. 1. Schematics of the quartz reactor used in experiments.

2.4. Analyses

After the furnace exposures, one sample of each material was prepared for material loss measurements and the other for measuring and characterizing the formed corrosion oxide scale.

The salt deposit was removed from the mass-loss samples, which were then washed in 20 ml reverse osmosis water using an ultrasound bath (Pro's Kit SS802) for 180 s. The samples were then dried and washed again using 20 ml 1 M HCl and ultrasound for 180 s. Finally, the samples were rinsed with distilled water and dried. After drying in a desiccator for 24 h, the samples were weighed three times. The material loss [mgcm^{-2}] was weighed and the thickness of the lost material [μm] was evaluated on the grounds of estimated density and the corroded surface area of the sample. The procedure will be addressed in greater detail in Sub-chapter 3.1.

Regarding the samples to be analyzed with SEM-EDS, a small amount of epoxy resin was put over the samples to hold the deposit in place and left to harden overnight. Next, the samples were cast in a chlorine-free epoxy resin and left to harden for 12 h. Then, the epoxy-embedded pieces were cut with a precision saw to expose the cross-sectional surface. The surface was polished and carbon-coated for SEM imaging and EDS analyses. The imaging of the cross-section was done with a scanning electron microscope equipped with an energy-dispersive X-ray (SEM-EDXA, Leo 1530 Gemini, Thermo Scientific UltraDry SDD X-ray detector). The EDS analyses were performed with a high-resolution FE-SEM (Thermo Scientific Apreo S), coupled with an energy-dispersive X-ray spectroscope (Oxford Instruments Ultim Max 100). The microscope was operated at an accelerating voltage of 20 kV.

The thickness of the formed corrosion oxide layer was determined by measuring the layer thickness in the SEM image from 20 separate places. The mean oxide layer thickness and standard deviation were calculated from these measurements.

2.5. Thermodynamic calculations

The melting behavior of the different salt mixtures was calculated using the thermodynamic software package Factsage, version 8.2. [18]. The thermodynamic data used for the calculations were then taken from the Fact Pure Substance (FactPS) database for stoichiometric compounds, as well as from the FTSalt database. The thermodynamic database for the molten salts considered alkali sulfates, chlorides, bromides, and fluorides, as well as the corresponding iron (II) salts ($FeSO_4$, $FeCl_2$, $FeBr_2$, FeF_2).

Two types of calculations were performed: a) melting behavior of the different alkali sulfate-halide mixtures as a function of temperature, and b) melting of the alkali salt mixtures at constant temperature (500, 550, 600 °C) when the corresponding iron halide is added to the mixture.

3. Results and discussion

3.1. Weight change and oxide thickness measurements

The oxidation rates of steels can be evaluated qualitatively compared with one another by measuring the sample's mass change [19] or the thickening of the oxide layer [20]. The thickness of the oxide layer has been reported to be proportional to the mass loss of the steel [i.a. 21]. Typically in cases with iron- and chromium-based alloys, the rate of corrosion is controlled by the diffusion of gaseous species through the oxide layer and follows the parabolic rate law [20]. However, it is known that both the temperature and the composition of the steel affect the details of the time-dependent corrosion of different steels [6,12,22–25]. In general, the rate of corrosion increases with increasing temperature, but again, the magnitude of the change depends on the composition of the steel [6,22,24–28]. The corrosion behavior of steel can change dramatically as a function of temperature even at temperatures below the melting point of the salt. Interestingly, the temperature affects not only the magnitude of corrosion, but also the type of degradation, e.g., metal loss, irregularities at the oxide/metal interface, and the depth of internal attack [28]. All the measured and calculated results addressing the mass change and oxide thickness are presented in Table 2. For the samples with either an oxide thickness or mass change below the detection limit, the term *nd* (not detected) has been given in the table. These samples are also not further discussed in the paper. On a qualitative level, the trend in mass loss correlates fairly well with the trend in oxide thickness. For example, with the $K_2SO_4 + Na_2SO_4 + KBr$ mixture, both the mass loss and oxide thickness increase as functions of temperature. Similarly, when comparing the three studied alloys with one another, the general trend in increasing mass loss and oxide thickness is Sanicro < AISI 347 < 10CrMo9-10. When noticing the amount of chromium and nickel, two key elements in terms of corrosion resistance, in the alloys, this is an expected result. However, the relative difference between the two samples depends on the mass loss or oxide thickness which has been measured. For example, with the $K_2SO_4 + Na_2SO_4 + KCl$ mixture, the measured mass loss of the 10CrMo9-10 at 550 °C is around 7.5 times higher than at 500 °C. The ratio is only around 2, when measured from the oxide thickness. This indicates that the qualitative correlation between the two different estimation methods is good, but finding a quantitative correlation might not be straightforward.

3.2. Material loss

The material loss [mgcm^{-2}] was calculated as an average for the top area of the sample (20x20mm) since the corrosion seemed to be quite uniform over the top area. The biggest material loss compared to the reference salt was measured for the 10CrMo9-10 steel at 550 °C with $K_2SO_4 + Na_2SO_4 + KCl$ salt and was roughly 20 times bigger than what was caused by the halide-free reference salt. The second largest material loss, roughly 10 times bigger compared to that induced by the reference salt, was caused by the $K_2SO_4 + Na_2SO_4 + KBr$ salt at both 550 °C and 600 °C. The mass losses measured for the $K_2SO_4 + Na_2SO_4 + KF$ salt were close to those measured for the reference salt in all tested temperatures. When comparing the three studied materials, the mass loss increased, as expected, in series Sanicro 28 < AISI 347 < 10CrMo9-10 and with increasing temperatures of 500 °C < 550 °C < 600 °C.

Starting from the weighed [mg] and calculated [mgcm^{-2}] material, the amount of metal [μm] that had been oxidized and thereby removed

Table 2
Measured and calculated test results of all samples, temperatures, and salt mixtures.

Salt	Sample	Measured mass loss [mgcm^{-2}]			Calculated material loss [μm]			Measured oxide thickness [μm]		
		500 °C	550 °C	600 °C	500 °C	550 °C	600 °C	500 °C	550 °C	600 °C
K_2SO_4 Na_2SO_4	10CrMo9-10	7,0	5,3	15,4	8,8	6,7	19,3	8,7	5,7	12,0
	AISI 347	nd	nd	nd	nd	nd	nd	nd	nd	nd
	Sanicro28	nd	nd	nd	nd	nd	nd	nd	nd	nd
K_2SO_4 Na_2SO_4 KCl	10CrMo9-10	14,3	106,6	101,1	17,9	133,3	126,4	67,7	130,0	115,7
	AISI 347	0,6	31,5	52,9	0,7	39,4	66,1	11,0	31,6	120,0
	Sanicro28	nd	14,3	25,0	nd	17,9	31,2	nd	30,0	25,8
K_2SO_4 Na_2SO_4 KBr	10CrMo9-10	10,0	45,3	128,5	12,5	56,6	160,6	33,6	110,0	130,0
	AISI 347	0,8	3,3	27,8	1,0	4,2	34,8	2,6	8,2	29,1
	Sanicro28	nd	0,7	3,0	nd	0,8	3,7	nd	3,1	5,6
K_2SO_4 Na_2SO_4 KF	10CrMo9-10	6,4	8,0	15,7	8,0	10,0	19,6	4,8	10,7	35,1
	AISI 347	nd	0,6	0,4	nd	0,7	0,5	nd	6,7	5,5
	Sanicro28	nd	0,5	nd	nd	0,6	nd	nd	nd	nd

nd = not detected.

in the etching process was also roughly estimated. This was carried out by first recording the mass loss of the sample and then calculating the material loss on the grounds of the density of the alloy and the volume of the removed material. It should be noted that the two values; metal loss and oxide thickness, do not match numerically. However, the idea was to measure the extent of corrosion in two different ways and see if the results show similar trends with both approaches. The comparison between the estimated oxidized metal and the measured corrosion oxide thickness for KCl and KBr of all materials at all temperatures is shown in Table 2 and Fig. 2. Unlike Table 2 which presented the entire test matrix, Fig. 2 summarizes only the cases where material loss and/or oxide thickness was measurable. It can be seen that the material loss follows the trend as expected: it increases as a function of temperature and is inversely proportional to the alloying degree. Furthermore, the calculated material loss corresponds well with the oxide layer thickness measured from the SEM images. The higher values of the measured thicknesses compared to the calculated loss can be contributed to the high porosity of the formed oxide layer, especially at low temperatures. The morphologies and compositions of the formed oxides will be discussed later in the text.

3.3. Oxide layer composition and thickness

Generally, as seen in Fig. 2, the thickness of the corrosion oxide scale increased in lower-alloyed materials and as a function of temperature. Depending on the studied material and temperature, the structure of the scale varied from a thin monoscale to a multi-layered scale. The multi-layered scales were detected only with the 10CrMo9-10 alloy (Fig. 3).

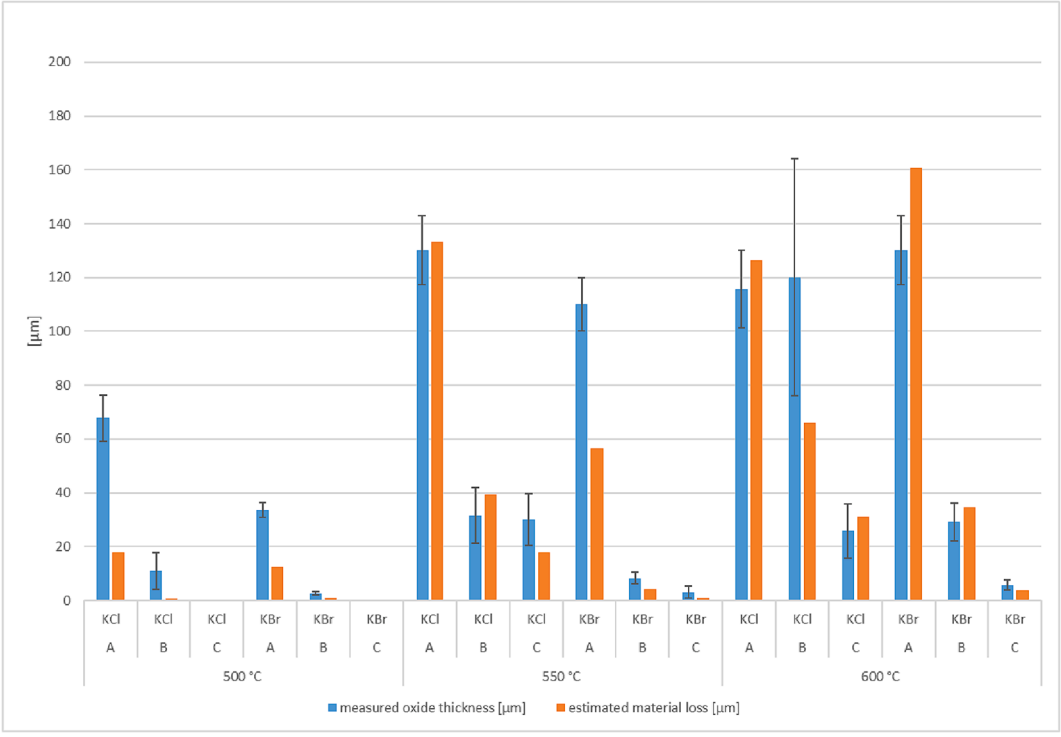

Fig. 2. Measured oxide thickness [μm] (from SEM images) and estimated material loss [μm] (from weight loss) of the samples exposed at 500, 550, and 600 °C exposed for 168 h to the mixtures containing either KCl or KBr. The labels A, B, and C stand for 10CrMo9-10, AISI347, and Sanicro28, respectively.

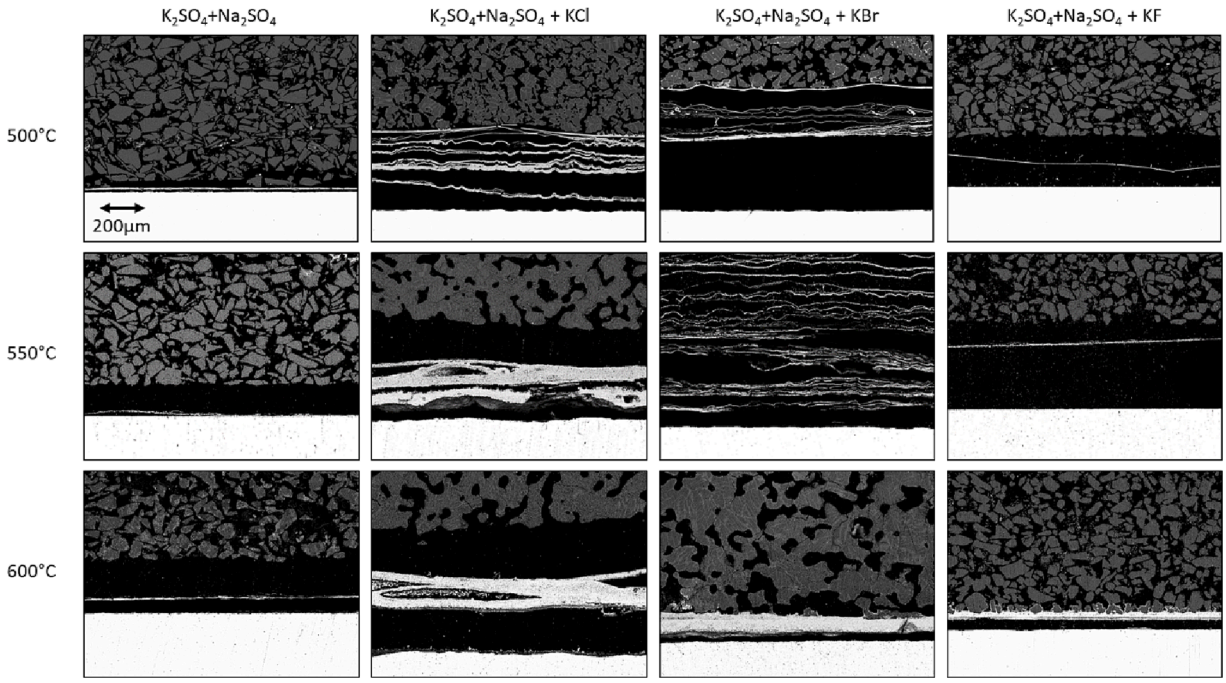

Fig. 3. Cross-sectional SEM images of 10CrMo9-10 steel in the presence of all the tested salts and at all temperatures. The temperature and salt mixture are indicated in the image. The magnification is the same for all images; the scalebar is seen in the first image.

3.3.1. 10CrMo9-10

At 500 °C, the lowest test temperature, the layer thicknesses could be measured only for 10CrMo9-10 with every salt mixture. Interestingly, the oxide structure was different in samples exposed to the reference salt or KF than in samples exposed to KCl or KBr. With the two first salts, the oxide consisted of one layer (≈ 9 µm and 5 µm) for the reference salt and the $K_2SO_4 + Na_2SO_4 + KF$ salt), whereas a multilayered oxide formed in the presence of the two latter salts (≈ 68 µm for the $K_2SO_4 + Na_2SO_4 +$ KCl salt; ≈ 34 µm for the $K_2SO_4 + Na_2SO_4 +$ KBr salt) (Figs. 2 and 3).

At 550 °C, the oxide structure was again different in samples exposed to the reference salt or KF than in samples exposed to KCl or KBr. With the two first salts, the oxide consisted of one layer (≈ 6 µm for the reference salt; ≈ 11 µm for the $K_2SO_4 + Na_2SO_4 + KF$ salt), whereas a multilayered oxide formed in the presence of the two latter salts (≈ 130 µm for the $K_2SO_4 + Na_2SO_4 +$ KCl salt; ≈ 110 µm for the $K_2SO_4 + Na_2SO_4 +$ KBr salt) (Figs. 3 and 4). In the case of KCl, separate layers had already started to grow together, forming a thick and more uniform oxide scale. The formation of a multilayered corrosion oxide on low-alloyed steel has been reported earlier [29–31] and is most likely related to iron chloride/bromide ($FeCl_x/FeBr_x$) formation. As potassium halide reacts with iron, the halide is released and it reacts with iron, forming a solid iron halide, which then easily vaporizes due to its high vapor pressure at 550 °C. As the gaseous iron halide diffuses toward a higher oxygen partial pressure, it will oxidize rapidly, and in the case of an unlimited supply of the halide, the reaction described above will repeat itself, resulting in a multilayered structure.

At 600 °C, a thin monolayer (~12 µm) formed in the presence of the reference salt, but the KF addition resulted in a thicker scale (35 µm). KCl and KBr both induced the growth of a thick and more uniform scale with thicknesses of 116 µm and 130 µm, respectively.

3.3.2. Aisi 347

At 500 °C, no measurable oxide formed on the AISI 347 sample beneath the reference salt or the $K_2SO_4 + Na_2SO_4 + KF$ salt. In the case of the $K_2SO_4 + Na_2SO_4 +$ KCl and $K_2SO_4 + Na_2SO_4 +$ KBr salts, oxide layers of ≈ 11 and 3 µm formed, respectively.

At 550 °C, no measurable oxide formed on the AISI 347 sample beneath the reference salt, and only a thin oxide (≈ 7 µm) formed beneath the $K_2SO_4 + Na_2SO_4 + KF$ salt. In the case of the $K_2SO_4 + Na_2SO_4 +$ KCl and $K_2SO_4 + Na_2SO_4 +$ KBr salts, oxide layers of ≈ 32 µm and ≈ 8 µm formed, respectively. Additionally, signs of salt particle sintering, such as rounding of sharp edges and bridging of the salt

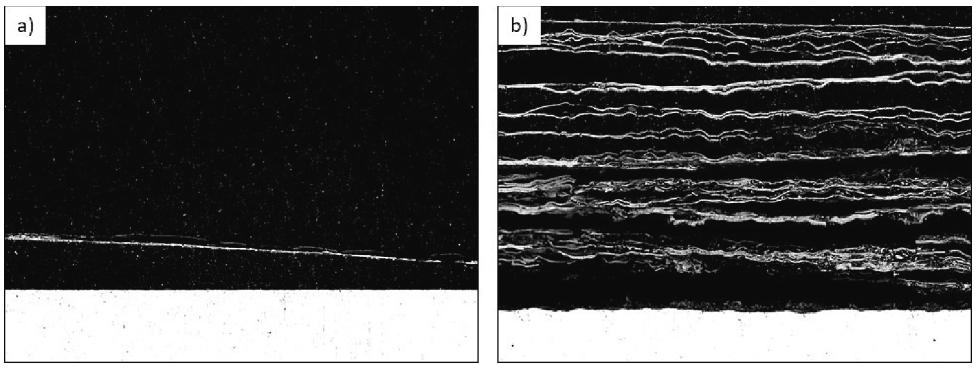

Fig. 4. Examples of 10CrMo9-10 steel exposed at 550 °C with a single-layered oxide formed in the presence of the reference $K_2SO_4 + Na_2SO_4$ salt (a) and a multi-layered oxide formed in the presence of the $K_2SO_4 + Na_2SO_4 +$ KBr salt (b).

particles were observed: in the case of the $K_2SO_4 + Na_2SO_4 + KBr$, the salt particles had sintered to some extent, whereas the sintering was more pronounced among the $K_2SO_4 + Na_2SO_4 + KCl$ salt particles. At 600 °C, the reference salt induced none and KF a thin scale with a thickness of ~ 6 μm. Similar to 550 °C, KCl and KBr induced thicker oxide layers of 120 μm and 29 μm, respectively. Significant sintering was also observed in the particles of both salt mixtures.

3.3.3. Sanicro 28

At 500 °C, no measurable oxide formed on the Sanicro 28 sample beneath any salt or at 550 °C in the cases with the reference salt or the $K_2SO_4 + Na_2SO_4 + KF$ salt. A very thin oxide scale with a uniform thickness of <5 μm formed in the presence of the $K_2SO_4 + Na_2SO_4 + KBr$ salt. Similar to the AISI 347 steel under the same conditions, the salt particles had sintered to some extent. The reaction with the $K_2SO_4 + Na_2SO_4 + KCl$ salt was more pronounced: the formed oxide was clearly thicker, and the thickness varied greatly (Fig. 5). The large thickness variation made it challenging to estimate the oxide scale thickness, which was below 5 μm at its thinnest (Spot A in Fig. 5) and above 80 μm in the thickest regions (Spot B in Fig. 5). Average thickness was 30 μm. Minor signs of sintering were observed between the $K_2SO_4 + Na_2SO_4 + KBr$ salt particles, whereas sintering was more pronounced between the $K_2SO_4 + Na_2SO_4 + KCl$ salt particles, which can be seen in Fig. 5. At 600 °C, no measurable oxide layer was detected beneath the reference salt and in the presence of the $K_2SO_4 + Na_2SO_4 + KF$ salt. For the $K_2SO_4 + Na_2SO_4 + KCl$ salt, a thicker oxide (26 μm) formed, whereas, in the presence of the $K_2SO_4 + Na_2SO_4 + KBr$ salt, a thin oxide (6 μm) was measured.

3.3.4. Remarks on the results

Among the studied heat-transfer materials, a thinner oxide indicates better corrosion resistance, which can be attributed to the chromium content of the alloy. Steels with high chromium content usually exhibit good oxidation resistance, and severe corrosion is avoided as long as selective oxidation of chromium is maintained. For the growth of the protective oxide layer to be maintained, the steel must be able to supply chromium from the bulk steel at a rate sufficient to balance the rate at which chromium is consumed in forming new oxide [32]. The chromium supply takes place via temperature-dependent diffusion along the grain boundaries, so the chromium concentration in the oxide increases with temperature. This means that the ability of a steel to resist uncontrolled oxidation depends on the concentration of chromium in the steel, the bulk diffusivity of chromium in the steel, and the grain size in the steel [33].

3.4. Melting behavior of the studied salts

When estimated with both applied methods (mass loss vs. oxide thickness), the corrosivity of the studied salts grew in series $K_2SO_4 + Na_2SO_4 + KF < K_2SO_4 + Na_2SO_4 + KBr < K_2SO_4 + Na_2SO_4 + KCl$. When studied as pure halides, KF was found to be the most corrosive before KCl and KBr [11]. The reason for the different order in corrosivity cannot be unambiguously explained within the frames of the current study, but the higher reactivity of the $K_2SO_4 + Na_2SO_4 + KBr$ and $K_2SO_4 + Na_2SO_4 + KCl$ salts could originate from the fact that the first melting temperature (T_0) of these salts is below 550 °C, while it is above 680 °C for $K_2SO_4 + Na_2SO_4 + KF$ (Fig. 6). The predicted and measured solidus temperatures or first melting temperatures (T_0) are listed in Table 3. The melt formation caused by only a 0.85 mol% addition of KCl or KBr could explain the higher reactivity of these two salts. This observation emphasizes nicely how important the knowledge of the melting behavior of genuine deposits on heat-transfer surfaces is when the corrosivity of such deposits is under investigation. Furthermore, when mixed with KCl (melting point 770 °C), iron chloride lowers the T_0 close to 350 °C [34,35]. When $FeCl_2$ or $FeBr_2$ forms in a reaction between the steel and alkali halide, it can further dramatically lower the T_0 of a KCl-containing deposit locally, thus initiating more severe corrosion through melt formation at temperatures lower than maybe expected. Furthermore, as

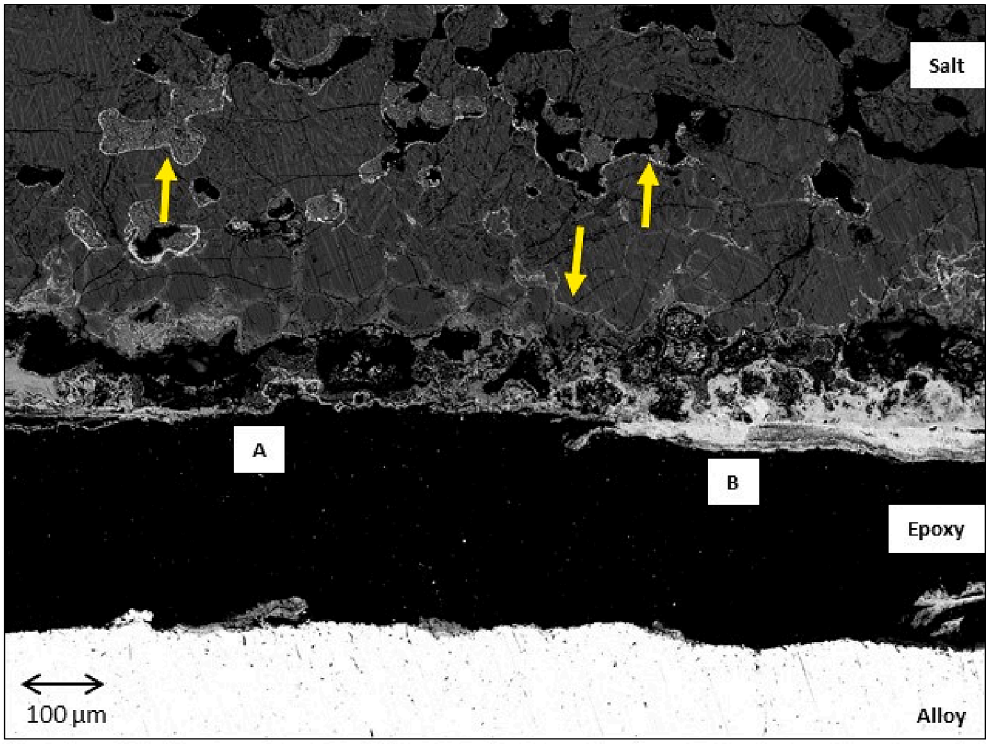

Fig. 5. A cross-sectional SEM image of Sanicro 28 sample exposed at 550 °C to the salt mixture containing KCl. The thin (A) and thick (B) regions of the formed oxide scale as well as areas with iron oxide (yellow arrows) inside the sintered salt have been indicated in the figure. (For interpretation of the references to colour in this figure legend, the reader is referred to the web version of this article.)

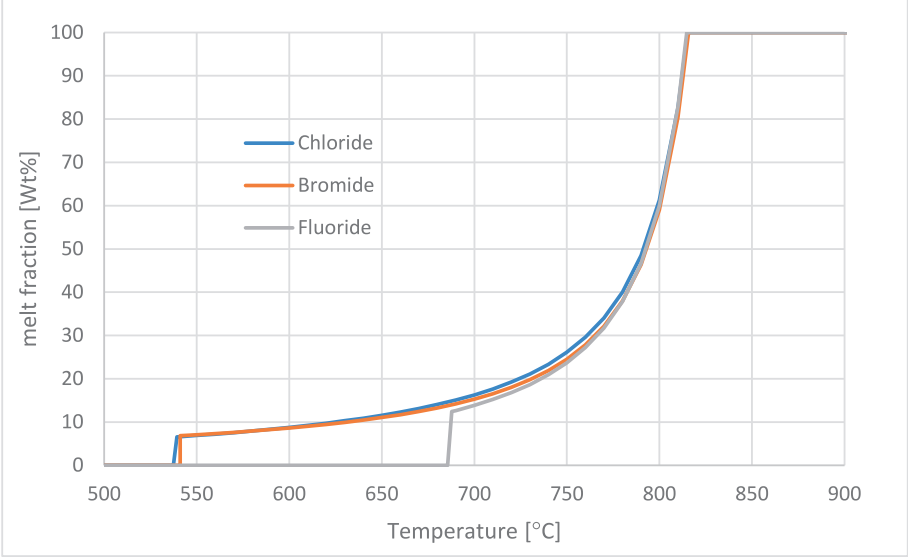

Fig. 6. The calculated melt fractions for the studied salt mixtures as functions of temperature.

Table 3
The predicted and measured solidus temperatures or first melting temperatures (T_0) of the studied salt mixtures.

Salt	$T_{0\ calc}$ [°C]	$T_{0\ meas}$ [°C]
$K_2SO_4 + Na_2SO_4$	834	838
$K_2SO_4 + Na_2SO_4 + KCl$	537	524
$K_2SO_4 + Na_2SO_4 + KBr$	541	549
$K_2SO_4 + Na_2SO_4 + KF$	686	698

shown with the thermodynamic calculations, the formation of very small amounts of $FeCl_2$ and $FeBr_2$ is already enough for melt formation at temperatures as low as 500 °C (Fig. 7). For the effect of iron halide addition, the chloride- and bromide-containing mixtures were predicted to melt to a larger extent if the corresponding iron halide content is increased, whereas no effect of FeF_2 was predicted on the melting behavior at the studied temperatures.

3.5. Effect of salt mixtures

3.5.1. Reference $K_2SO_4 + Na_2SO_4$ salt

A very thin oxide scale with an outer iron oxide and an inner oxide layer of iron together with a chromium content higher than in the unreacted alloy formed on 10CrMo9-10 at 550 °C and 600 °C. At 600 °C, a thin duplex-structured oxide layer with an iron-rich outer and an inner iron-chromium spinel ($FeCr_2O_4$) layer formed on AISI 347. However, the oxide formation did not originate from the sulfate salt, since these alloys are known to oxidize at studied temperatures [36]. The duplex structure of the oxide originates from the faster diffusion of iron outwards, resulting in an iron-rich oxide scale at the surface, while chromium is oxidized underneath this scale by the inward diffusion of oxygen.

3.5.2. The effect of fluorine

Although the addition of KF did not result in higher mass losses or thicker oxides than in the case with the reference salt, a few interesting features originated from the presence of KF. A structurally similar thin oxide scale formed on all three studied materials at 600 °C. In the case of the two higher-alloyed materials (AISI 347 and Sanicro 28), an iron-rich outer and an inner $FeCr_2O_4$ layer formed, whereas the inner iron oxide layer of the lower-alloyed 10CrMo9-10 was chromium-rich only when compared with the unreacted bulk material. Interestingly, iron, most likely as iron oxide, was identified around the salt particles closest to the formed oxide (Fig. 8). Furthermore, minor signs of salt particle sintering were observed visually with rounding of sharp edges and bridging between particles. The signs of sintering and the presence of iron around the salt particles suggest the formation of a volatile iron compound. However, iron fluorides FeF_2 and FeF_3 require quite high temperatures to reach significant vapor pressures [37]. Since iron was detected only on salt particles, which were in physical contact with the oxide scale, another option for the transport mechanism of iron could be iron fluoride migration by the capillary effect without the formation of gaseous species containing iron. Traces of fluorine and initial signs of grain boundary attack (not shown here) were detected beneath the oxide formed on the alloy Sanicro 28. The presence of grain boundary attack and fluorine at the scale/alloy interface has been reported earlier to occur in experiments with pure KF [11].

Although the authors could not find Gibbs free energy of formation for FeF_3, when Fe reacts with KF, it has been reported that FeF_3 forms when F_2 reacts with either Fe or Fe_2O_3 [38,39]. Another suggested F-containing species, which could have formed, is chromium fluoride [11]. Regardless of the small amount of KF present in the current study, the similarities with the samples exposed previously to pure KF at the same temperatures [11]. suggest that the corrosion mechanism was the same in both studies and that material degradation was initiated by the presence of KF.

3.5.3. The effect of bromine

The addition of Br to the reference salt clearly changed the scale morphology in the case of alloy 10CrMo9-10. Several separate oxide layers formed at 500 °C and 550 °C, while a more contiguous scale formed at 600 °C. Including every separate layer, the oxide consisted of an iron-rich outer and a chromium-rich (when compared to the surroundings) inner layer. Iron oxide was found around the salt particles closest to the steel surface at all tested temperatures. Furthermore, traces of Br and S were detected underneath the oxide scale formed at 600 °C. In the cases with the higher-alloyed materials AISI 347 and Sanicro 28, the oxide scale consisted of an iron-rich outer and a chromium-rich inner layer. This duplex layer originates from the high solubility of iron in Cr_2O_3, which permits the outward diffusion of iron and the formation of the outermost iron-rich oxide layer. Again, iron oxide was found around the salt particles closest to the steel surface, in addition to which traces of S were detected underneath the oxide scale together with a Ni-rich zone (Fig. 9). Furthermore, at 600 °C, pits with Fe/Cr oxides and Ni enriched at the pit edges were detected in the alloy

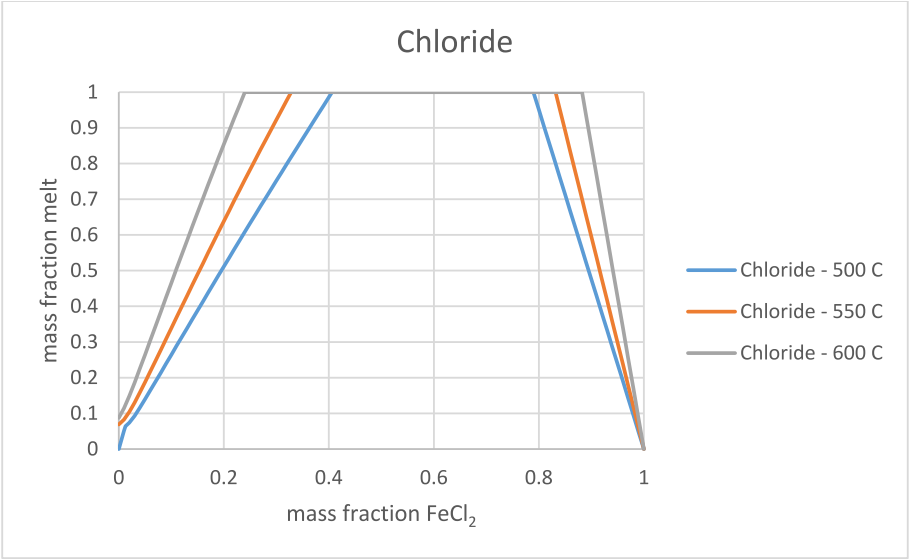

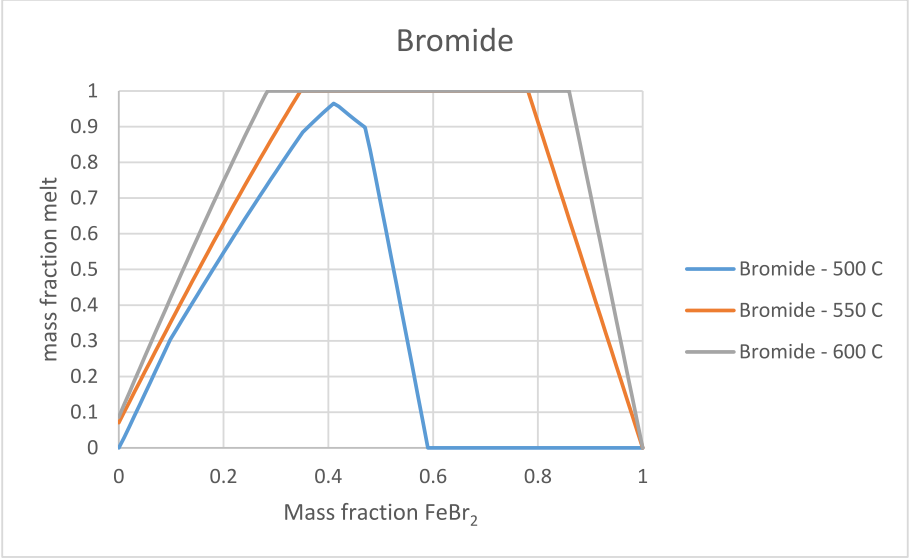

Fig. 7. The calculated melt fractions for the iron halides in the salt mixtures as functions of a mass fraction.

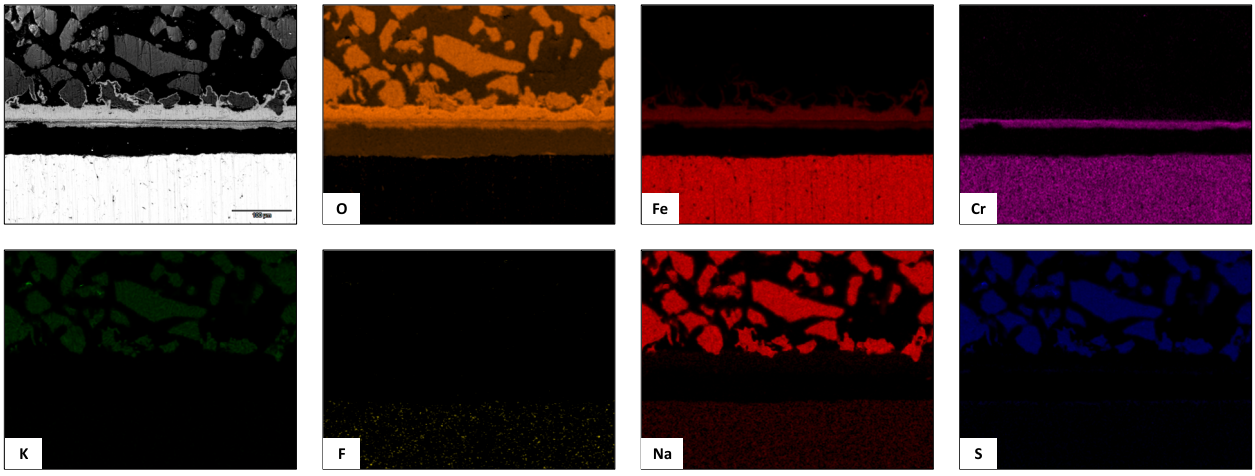

Fig. 8. SEM-EDS elemental maps for alloy 10CrMo9-10 exposed for 168 h at 600 °C in the presence of the $K_2SO_4 + Na_2SO_4 + KF$ salt.

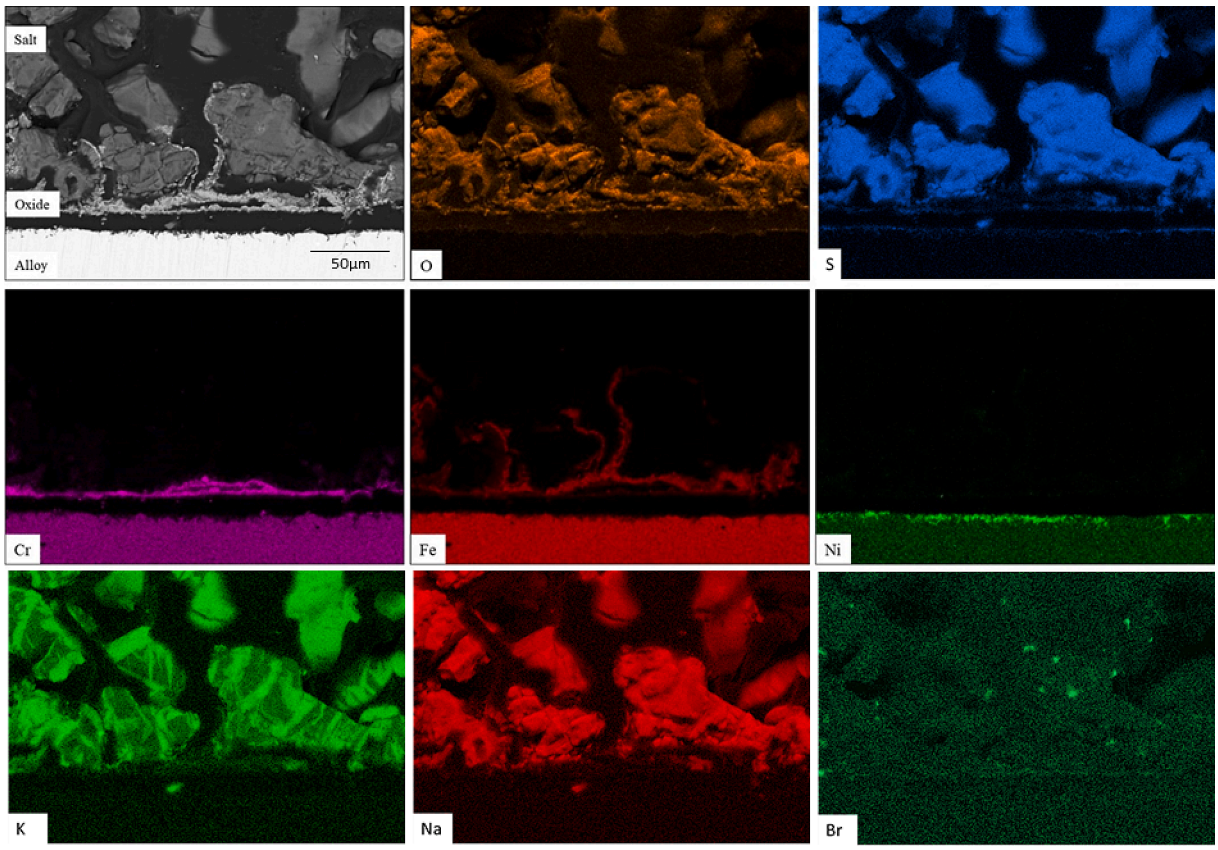

Fig. 9. SEM-EDS elemental maps for alloy AISI 347 exposed for 168 h at 550 °C in the presence of the $K_2SO_4 + Na_2SO_4 + KBr$ salt.

AISI 347, but there was no evidence of S or Br in the pits.

At the studied temperature range, a uniform oxide scale forms on the steel 10CrMo9-10 in the absence of salt [36]. The observed multilayered scales suggest that KBr plays a role in alloy oxidation. Keeping in mind the high Fe concentration of 10CrMo9-10, bromine reacted, most likely rather as a bromide ion than molecular bromine gas, with iron in the uppermost layers of the steel, forming iron bromides ($FeBr_x$). In the presence of either KBr [31] or gaseous bromine [40], iron bromides have been identified to have formed in iron-based steels at the oxide/alloy interface at 550 °C and 700 °C. However, iron bromide is not stable, but oxidizes due to the high enough oxygen partial pressure. The rapid oxidation resulted in porous oxide layers, which could not prevent additional bromine to pass through the layers. Beneath these layers, the oxygen partial pressure was presumably low enough for iron bromide formation and as the formed iron bromides volatilized toward higher oxygen partial pressures, new thin iron oxide layers formed, explaining the multilayered oxide structure imaged in Fig. 4b. The bromine detected beneath the formed oxide at 600 °C further supports the idea of accelerated oxidation through metal bromide formation.

In principle, the reaction mechanism between KBr and one of the higher-alloyed materials is the same as in the case with 10CrMo9-10, but due to the higher chromium content, the formation of Cr-containing intermediates such as potassium chromate (K_2CrO_4) and chromium bromides ($CrBr_x$) cannot be excluded. Since the standard enthalpies of formation for iron and chromium bromides are very close to one another [41], it is difficult to estimate whether only one or both bromides formed. However, the higher vapor pressure of $FeBr_x$ at the studied temperatures [37] and the formation of iron oxide around the salt particles suggest that iron bromide has been the main intermediate. At a slightly higher temperature (700 °C), when FeCr- and FeNi-based commercial alloys were exposed to a Br-containing gas, $FeBr_3$ was reported to form first at the steel/oxide interface, followed by the formation of $FeBr_2$, $CrBr_3$, and $NiBr_2$ [40]. In the present study, the Ni enrichment at the scale/alloy interface suggests the selective bromination/oxidation of iron and chromium. In the case of alloys rich in chromium, potassium from KBr can react with chromium, forming K_2CrO_4, which reacts further to non-protective chromium oxide [31]. The formation of K_2CrO_4 will slowly deplete the region beneath the oxide scale in chromium and when no chromium can diffuse toward the alloy surface to replace the oxidized chromium, the alloy can no longer form a protective oxide, resulting in breakaway oxidation. Since the added amount of KBr in the present study was small, the formation of K_2CrO_4 could not be unambiguously verified. However, the formation of K_2CrO_4 should be kept in mind when mechanisms for material degradation are considered.

3.5.4. *The effect of chlorine*

In terms of chemical compositions, the addition of Cl to the reference salt resulted in similar scale structures as in the case of the Br addition. The multilayered scale formed on steel 10CrMo9-10 at all tested temperatures consisted mainly of iron with traces of chromium on the alloy side of each oxide layer. Furthermore, Cl with no K was detected underneath the oxide layer closest to the alloy surface. The multilayered structure together with Cl at the scale/alloy interface suggests that the reaction mechanism has been analogous to that with the KBr addition. Since the iron content of the steel was high and the vapor pressure of iron chloride ($FeCl_x$) sufficient, volatilizing iron chlorides formed at low oxygen partial pressures were stable and diffused outward, oxidizing either at the scale surface or onto the salt particles closest to the alloy surface. As the formed oxide layers did not provide any protection to the underlying steel and due to the chlorine reservoir in the salt mixture, chlorine diffused over and over again to the alloy surface, where it reacted repeatedly forming first volatilizing iron chlorides and, after having diffused outward, iron oxide layers.

An oxide scale with an iron-rich outer part and a chromium-rich

inner part formed on the two higher-alloyed materials. The structure can partly be explained by the higher diffusivity of iron compared to that of chromium in an FeCr steel [42], resulting in faster iron transportation towards the steel surface, where the oxide scale forms. Since Fe_2O_3 and Cr_2O_3 are structurally isotypic and the spinel-type Fe_3O_4 dissolves chromium forming a mixed spinel $FeCr_2O_4$ [43], it was not possible to differentiate these oxides from one another in this study. However, iron oxide was identified around the salt particles closest to the sample surface, indicating outward diffusion of iron, most likely as volatile iron chloride. As mentioned before, the oxidation of iron chloride is rapid, resulting in a porous oxide scale, which cannot prevent the transportation of reactive species to the alloy surface and away from it. Chlorine was again found underneath the formed oxide, further supporting the active role of chlorine in material degradation. Nickel remained immobile and was found enriched in the region beneath the scale/alloy interface (Fig. 10). Similarly, to the reactions with KBr, Cr-containing alloys have been reported to form K_2CrO_4 in reactions with KCl [e.g. 44]. Chromate formation will deplete the protective oxide in chromium, which will eventually lead to faster chlorine penetration through the oxide scale and through that, accelerated corrosion.

In addition to chlorine, sulfur was identified beneath the formed oxide, where it diffused through the porous scale. At 600 °C, sulfur-containing molten salt mixtures have been reported to corrode nickel-based alloys through nickel sulfate ($NiSO_4$) formation [45]. In the present study, the sintering of the particles and formation of low-melting metal chlorides have established conditions, under which sulfur-induced corrosion might have occurred to some extent. However, corrosion of alloys AISI 347 and Sanicro 28 has mainly originated from the interaction between KCl and the studied alloys.

4. Conclusions

In this study, the corrosivity of three different salt mixtures ($K_2SO_4 + Na_2SO_4 + KBr$, $K_2SO_4 + Na_2SO_4 + KCl$, and $K_2SO_4 + Na_2SO_4 + KF$) was compared to a halide-free reference carrier in exposures of three commercial heat-transfer materials (10CrMo9-10, AISI 347, and Sanicro 28) typically used in different parts of a biomass- and/or waste-fired boiler. The tube furnace exposures were carried out at 500, 550, and 600 °C for 168 h in a flowing air atmosphere. After the exposure, the mass loss of each sample was recorded, and it was compared with the thickness of the formed oxide layer. The idea was to explore whether the results from two different kinds of corrosion measurement approaches can be compared with one another. Based on the results of the study, the following conclusions can be made:

- The corrosivity of the salts increased in order $K_2SO_4 + Na_2SO_4 + KF < K_2SO_4 + Na_2SO_4 + KBr < K_2SO_4 + Na_2SO_4 + KCl$.
- Regardless of the studied salt, the corrosion resistance of the studied alloys grew in series 10CrMo9-10 < AISI 347 < Sanicro 28. This can be attributed to the Cr and Ni contents of the alloy; the higher the amounts of Cr and Ni in the alloy, the better the corrosion resistance.
- Already small amounts of corrosive salts in an inert carrier change significantly the corrosion and melting behavior of the salt mixture.
- Such drastic changes in the melting behavior of the deposit can be significant in practical applications such as boilers.
  - o In this study, a good example is the KF addition, which didn't accelerate corrosion but did influence the migration of iron from the steel onto the closest salt particles.
- On a qualitative level, the same results were obtained with both corrosion measurement methods (mass loss vs. oxide thickness). However, especially in the case of porous oxides forming as a result of metal halide volatilization, caution must be taken when giving numeric values for the measured oxide thickness.
- Material loss experiments give clear and consistent corrosion results but during the sample preparation after the exposure, one loses all chemical information regarding the corrosion oxide layer. Hence, "a double method" (one sample for the mass loss and another one for the cross-section analyses) should be considered to regain the maximal amount of information.

CRediT authorship contribution statement

J.-E. Eriksson: Conceptualization, Methodology, Formal analysis, Writing – original draft. **J. Lehmusto:** Conceptualization, Methodology, Formal analysis, Writing – original draft, Writing – review & editing, Supervision, Project administration, Funding acquisition. **M. Dirbeba:** Methodology. **L. Silvander:** Formal analysis. **D. Lindberg:** Formal analysis. **L. Hupa:** Writing – review & editing.

Declaration of Competing Interest

The authors declare that they have no known competing financial interests or personal relationships that could have appeared to influence the work reported in this paper.

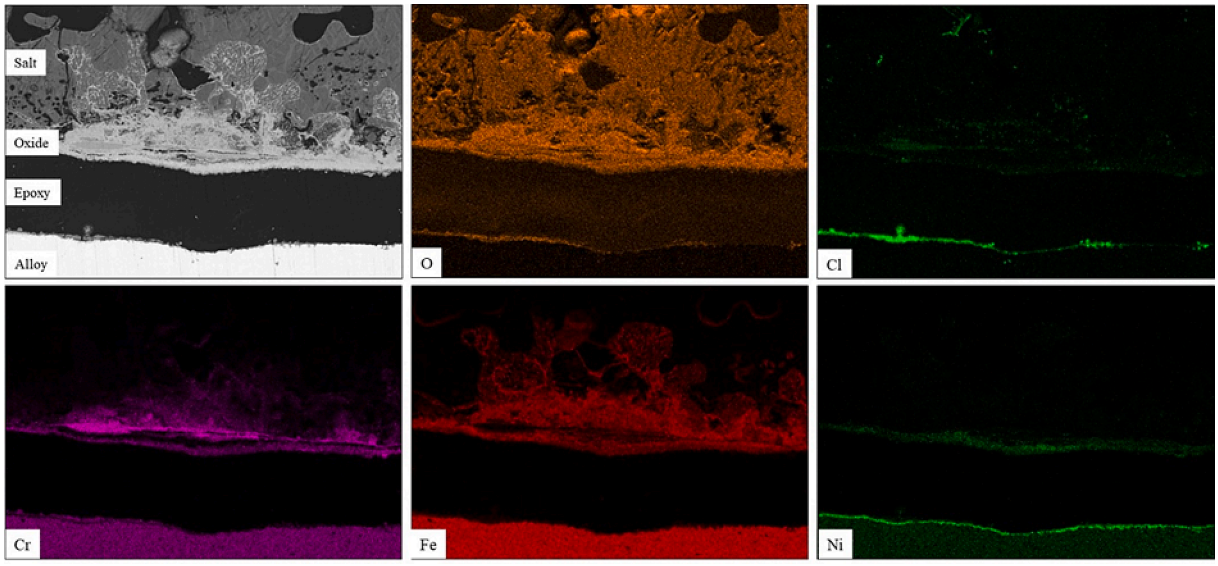

Fig. 10. SEM-EDS elemental maps for alloy AISI 347 exposed for 168 h at 550 °C in the presence of the $K_2SO_4 + Na_2SO_4 + KCl$ salt.

Data availability

Data will be made available on request.

Acknowledgments

This work was conducted within the Academy of Finland project "Initiation and propagation of high-temperature corrosion reactions in complex oxygen-containing environments" (Decision no. 348963). This work was partly supported by the project Clean and efficient utilization of demanding fuels (CLUE^2), with support from the industrial partners: ANDRITZ Oy, Valmet Technologies Oy, UPM-Kymmene Oyj, Metsä Fibre Oy, and International Paper Inc., as part of the activities of the Åbo Akademi University Johan Gadolin Process Chemistry Centre.

References

[1] Brossard JM, Diop I, Chaucherie X, Nicol F, Rapin C, Vilasi M. Superheater fireside corrosion mechanisms in MSWI plants: lab-scale study and on-site results. Mater Corros 2011;62:543–8. https://doi.org/10.1002/maco.201005849.
[2] Enestam, S., Corrosivity of hot flue gases in the fluidized bed combustion of recovered waste wood, PhD Thesis, Åbo Akademi 2011.
[3] Hansen LA, Nielsen HP, Frandsen FJ, Dam-Johansen K, Hørlyck S, Karlsson A. Influence of deposit formation on corrosion at a straw-fired boiler. Fuel Process Technol 2000;64(1–3):189–209.
[4] Nielsen HP, Frandsen FJ, Dam-Johansen K, Baxter LL. The implications of chlorine-associated corrosion on the operation of biomass-fired boilers. Prog Energy Combust Sci 2000;26:283–98.
[5] Skrifvars B-J, Backman R, Hupa M, Salmenoja K, Vakkilainen E. Corrosion of superheater steel materials under alkali salt deposits Part 1: The effect of salt deposit composition and temperature. Corros Sci 2008;50(5):1274–82.
[6] Grabke HJ, Reese E, Spiegel M. The effects of chlorides, hydrogen chloride and sulfur dioxide in the oxidation of steels below deposits. Corros Sci 1995;37(7):1023–43.
[7] Krook J, Mårtensson A, Eklund M. Metal contamination in recovered waste wood used as energy source in Sweden. Resour Conserv Recycl 2004;41(1):1–14.
[8] Nakamura K, Kinoshita S, Takatsuki H. The origin and behavior of lead, cadmium and antimony in MSW incinerator. Waste Manag 1996;16(5–6):509–17.
[9] Belevi H, Moench H. Factors determining the element behavior in municipal solid waste incinerators. 1. Field studies. Environ Sci Tech 2000;34(12):2501–6.
[10] Vehlow J, Mark FE. Influence of bromine on metal volatilization in waste combustion. J Mater Cycles Waste Manage 2000;2(2):89–99.
[11] Wu H, Yrjas P, Hupa M. Laboratory studies of potassium-halide-induced high-temperature corrosion of superheater steels. Part 1: exposures in dry air. Energy Fuel 2015;29(2):1186–95.
[12] Spiegel M. Salt melt induced corrosion of metallic materials in waste incineration plants. Mater Corros 1999;50(7):373–93.
[13] Åmand L, Leckner B, Eskilsson D, Tullin C. Ash deposition on heat transfer tubes during combustion of demolition wood. Energy Fuel 2006;20(3):1001–7.
[14] Wu H, Bankiewicz D, Yrjas P, Hupa M. Laboratory studies of potassium halide-induced high-temperature corrosion of superheater steels. Part 2: exposures in wet air. Energy Fuel 2015;29(4):2709–18.
[15] Lehmusto J, Yrjas P, Skrifvars BJ, Hupa M. Detailed studies on the high temperature corrosion reactions between potassium chloride and metallic chromium. Mater Sci Forum 2011;696:218–23. https://doi.org/10.4028/www.scientific.net/MSF.696.218.
[16] Bankiewicz D, Vainikka P, Lindberg D, Frantsi A, Silvennoinen J, Yrjas P, et al. High temperature corrosion of boiler waterwalls induced by chlorides and bromides – Part 2: Lab-scale corrosion tests and thermodynamic equilibrium modeling of ash and gaseous species. Fuel 2012;94:240–50.
[17] Lehmusto J, Lindberg D, Yrjas P, Hupa L. The effect of temperature on the formation of oxide scales regarding commercial superheater steels. Oxid Met 2018;89(1-2):251–78.
[18] Bale CW, Bélisle E, Chartrand P, Decterov SA, Eriksson G, Gheribi AE, et al. FactSage thermochemical software and databases, 2010–2016. Calphad 2016;54:35–53.
[19] Pettersson J, Asteman H, Svensson J-E, Johansson L-G. KCl induced corrosion of a 304-type austenitic stainless steel at 600°C; the role of potassium. Oxid Met 2005;64(1–2):23–41.
[20] Nielsen HP, Frandsen FJ, Dam-Johansen K. Lab-scale investigations of high-temperature corrosion phenomena in straw-fired boilers. Energy Fuel 1999;13(6):1114–21.
[21] Cha SC. High temperature corrosion of superheater materials below deposited biomass ashes in biomass combusting atmospheres. Corros Eng Sci Technol 2007;42(1):50–60.
[22] Sánchez-Pastén M, Spiegel M. High temperature corrosion of metallic materials in simulated waste incineration environments at 300–600°C. Mater Corros 2006;57(2):192–5.
[23] Shinata Y, Nishi Y. NaCl-induced accelerated oxidation of chromium. Oxid Met 1986;26(3–4):201–12.
[24] Zahs A, Spiegel M, Grabke H. Chloridation and oxidation of iron, chromium, nickel and their alloys in chloridizing and oxidizing atmospheres at 400–700°C. Corros Sci 2000;42(6):1093–122.
[25] Pettersson J, Svensson J-E, Johansson L-G. KCl-induced corrosion of a 304-type austenitic stainless steel in O_2 and in O_2+H_2O environment: the influence of temperature. Oxid Met 2009;72(3–4):159–77.
[26] Shinata Y. Accelerated oxidation rate of chromium induced by sodium chloride. Oxid Met 1987;27(5–6):315–32.
[27] Folkeson N, Jonsson T, Halvarsson M, Johansson L-G, Svensson J-E. The influence of small amounts of KCl(s) on the high temperature corrosion of a Fe-2.25Cr-1Mo steel at 400 and 500°C. Mater Corros 2011;62(7):606–15.
[28] Weulersse-Mouturat K, Moulin G, Billard P, Pierotti G. High temperature corrosion of superheater tubes in waste incinerators and coal-fired plants. Mater Sci Forum 2004;461–464:973–80.
[29] Lehmusto J, Yrjas P, Skrifvars B-J, Hupa M. High temperature corrosion of superheater steels by KCl and K_2CO_3 under dry and wet conditions. Fuel Process Technol 2012;104:253–64.
[30] Larsson E, Gruber H, Hellström K, Jonsson T, Liske J, Svensson J-E. A comparative study of the initial corrosion of KCl and $PbCl_2$ on a low-alloyed steel. Oxid Met 2017;87(5-6):779–87.
[31] Lehmusto J, Bergelin M, Lill J-O. Production and use of radioactive [^{82}Br] KBr in high-temperature corrosion studies. Corros Sci 2019;148:24–30.
[32] Othman NK, Zhang J, Young DJ. Effect of water vapour on cyclic oxidation of Fe-Cr alloys. Mater Corros 2011;62(6):496–503.
[33] Asteman H, Svensson J-E, Johansson L-G. Evidence for chromium evaporation influencing the oxidation of 304L: The effect of temperature and flow rate. Oxid Met 2002;57(3–4):193–216.
[34] Levin EM, McMurdie HF, Reser MK. *Phase diagrams for ceramists* **Vol. III**, 1969, The American Ceramic Society, Westerville, Ohio, USA.
[35] Krause HH. *Corrosion by chlorine in waste-fueled boilers*, in: Bryers, R.W. (Ed.), Incinerating municipal and industrial waste, fireside problems, and prospects for improvement, 145-159, 1991, Hemisphere Publishing Corporation, Washington D. C., USA.
[36] Lehmusto J, Lindberg D, Yrjas P, Hupa L. The effect of temperature on the formation of oxide scales regarding commercial superheater steels. Oxid Met 2018;89:251–78.
[37] Lai GY. High temperature corrosion of engineering alloys. Materials Park, OH, USA: ASM International; 1990.
[38] Johnson GK. The enthalpy of formation of FeF_3 by fluorine bomb calorimetry. J Chem Thermodyn 1981;13(5):465–9.
[39] Zhou H, Ruther RE, Adcock J, Zhou W, Dai S, Nanda J. Controlled formation of mixed nanoscale domains of high capacity Fe_2O_3-FeF_3 conversion compounds by direct fluorination. ACS Nano 2015;9(3):2530–9.
[40] Lee S, Tsujikawa S. Corrosion behavior of Fe-Cr and Fe-Ni-base commercial alloys in flowing Ar-42.6%O_2-14.7%Br 2 gas mixture at 700 °C. Mater Corros 1997;48(6):364–71.
[41] Hisham MWM, Benson SW. Thermochemistry of inorganic solids. 7. Empirical relations among enthalpies of formation of halides. J Phys Chem 1987;91(13):3631–7.
[42] Lobnig RE, Schmidt HP, Hennesen K, Grabke HJ. Diffusion of cations in chromia layers grown on iron-base alloys. Oxid Met 1992;37(1-2):81–93.
[43] Young DJ. High temperature oxidation and corrosion of metals. 2nd ed. Amsterdam, Netherlands: Elsevier; 2016.
[44] Sui J, Lehmusto J, Bergelin M, Hupa M. The effects of KCl, NaCl and K_2CO_3 on the high-temperature oxidation onset of Sanicro 28 steel. Oxid Met 2016;85(5-6):565–98.
[45] Spiegel M. Influence of gas phase composition on the hot corrosion of steels and nickel-based alloys beneath a (Ca-Na-K)-sulfate mixture containing $PbSO_4$ and $ZnSO_4$. Mater Corros 2000;50(5):303–12.